



Synthesis and characterization of highly active $Pb_x@Pt_y/C$ core-shell nanoparticles toward glycerol electrooxidation



Lays S.R. Silva ^a, Franz E. López-Suárez ^a, M. Perez-Cadenas ^b, Sydney F. Santos ^c,
Luiz P. da Costa ^d, Katlin I.B. Eguiluz ^a, Giancarlo R. Salazar-Banda ^{a,*}

^a *Electrochemistry and Nanotechnology Laboratory, Research and Technology Institute/Processes Engineering Post-graduation – PEP, Universidade Tiradentes, Av. Murilo Dantas, 300, Aracaju, SE, Brazil*

^b *Department of Inorganic Chemistry and Technical, UNED, Faculty of Sciences, Senda del Rey no 9, 28040 Madrid, Spain*

^c *Center of Engineering, Modeling, and Applied Social Sciences, Universidade Federal do ABC, Av. dos Estados 5001, Santo André, SP, Brazil*

^d *Research and Technology Institute/Industrial Biotechnology Post-graduation – Universidade Tiradentes, Av. Murilo Dantas, 300, Aracaju, SE, Brazil*

ARTICLE INFO

Article history:

Received 1 February 2016

Received in revised form 7 April 2016

Accepted 23 April 2016

Available online 21 May 2016

Keywords:

Electrocatalysis

glycerol electrooxidation

scanning-transmission electron microscopy

x-ray photoelectron spectroscopy

fuel cells

ABSTRACT

In this manuscript we report the facile synthesis route and electrochemical evaluation of $Pb_x@Pt_y/C$ core–shell (CS) nanostructures (with $x:y$ molar ratios of 1:3, 1:2, 1:1 and 2:1) for glycerol electrooxidation reaction in acid media. Pb_xPt_y/C alloy nanoparticles were also synthesized with the same compositions of CS nanoparticles for comparative purposes. The as-prepared $Pb_x@Pt_y/C$ nanostructures were characterized by scanning transmission electron microscopy (STEM), high-resolution transmission electron microscopy, X-ray diffraction and X-ray photoelectron spectroscopy. Microscopy results indicate that CS nanoparticles were well-dispersed on carbon support, with spherical shapes and small particle sizes (2.6–3.9 nm). Deviations in the lattice parameter, as well as, in binding energies demonstrated interaction between Pt and Pb, leading to alterations of the surface atom electron densities that, in turn, influence the $Pb_x@Pt_y/C$ electroactivity. High-angle annular dark-field-STEM associated with line-scan energy dispersive X-ray spectroscopy indicate the formation of a core–shell type structure (Pt shell and Pb core) for the $Pb@Pt_3/C$ composition, which is in good agreement with the cyclic voltammetry (CV) experiments, where only the characteristic profile of polycrystalline Pt is observed. The catalytic activity towards glycerol oxidation was accessed by CV, chronoamperometry and quasi-stationary potentiostatic polarization. The CS nanostructures showed higher catalytic activities than those of the nanostructured alloys with similar chemical compositions, probably due to different surface structures combined with electronics effects. Moreover, the investigated CS nanostructures presented good durability. These results credited $Pb@Pt_3/C$ CS nanoparticles as potential catalysts in direct glycerol fuel cells (DGFC). Finally, we highlight that the investigated synthesis route is a facile and reproducible way for producing $Pb_x@Pt_y/C$ CS electrocatalysts, which is significant for the development of high performance DGFC.

© 2016 Elsevier B.V. All rights reserved.

1. Introduction

There is an increasing interest on fuel cells fed with alcohols (direct alcohol fuel cells or DAFC) for alternative energy generation [1–6]. Easy storage and handling, high-energy density, and wide availability are characteristics that make attractive the use of alcohols as power sources for mobile, stationary and portable appli-

cations [7]. Several different alcohols have been considered over the time for DAFC applications. One of the most studied is methanol [8,9] due to its low molecular weight, simple structure and high energy density (6.1 kWh Kg⁻¹) [10–12]. Nevertheless, the development of DAFCs based on methanol has serious difficulties to be overcome [13], such as high flammability and toxicity [14]. Another relevant aspect is the permeability of methanol through the Nafion membrane, which leads to methanol crossover from the anode to the cathode side [15]. This effect has serious consequences on the fuel cell efficiency, which, at low current densities, can be dramatically reduced by more than 50% [16]. Polyhydric alcohols such as glycerol has also been investigated as fuels in the DAFCs because they have high boiling points, lower toxicity than methanol and can be catalytically converted into energy through the oxidation

* Corresponding author.

E-mail addresses: lays.reis@yahoo.com.br (L.S.R. Silva), franzedwin@gmail.com (F.E. López-Suárez), mariaperez@ccia.uned.es (M. Perez-Cadenas), sydney.ferreira@ufabc.edu.br (S.F. Santos), lupeco7@hotmail.com (L.P. da Costa), katlin.eguiluz@pq.cnpq.br (K.I.B. Eguiluz), gianrsb@gmail.com (G.R. Salazar-Banda).

of their three hydroxyls (OH). Moreover, currently there is a large availability of glycerol in the market since it is the main by-product of biodiesel production. Therefore, glycerol final destination is a serious problem to be solved by biodiesel industry [17].

Many studies have been performed on the direct oxidation fuel cell using methanol, ethanol and ethylene glycol [18–21], however, the use of glycerol in fuel cell is on the beginning. The fuel cells fed with glycerol show high energy density like other fuels (8.1; 6.1; 5.7; 5.2 e 5.0 kWh Kg⁻¹ for ethanol, methanol, ammoniac, ethylene glycol and glycerol, respectively). The development of direct glycerol fuel cells is limited by the complexity of its oxidation reactions, i.e., this kind of alcohol (polyhydric) has a complex reaction mechanism due to the presence of C–C bond into the molecule, which, depending on the electrode surface and the supporting electrolyte, can undergo a variety of different reaction pathways with different active intermediates (compounds such as esters and free fatty acid having C=O group in their structure) and final products, which could inhibit or poison the metallic catalysts, reducing their catalytic activity, resulting in poor electrochemical performance and low energy efficiency [3]. The reaction steps preceding the rate-determining step in the electrooxidation of glycerol involve the C–C bond cleavage. The most likely sequence for such reactions requires a number vacant active sites to produce three CO complexes bonded to the surface of a given material per mole of glycerol [22,23].

The high activity and stability of Pt metal, especially under acidic environment, makes it a suitable catalyst for electrooxidation of many small organic molecules. Despite of the impressive properties of Pt, the high cost of this noble metal motivates huge research efforts for developing high active electrocatalysts with low loading of this metal. Kim et al. [24] studied the electrooxidation of ethylene glycol and glycerol 0.2 M in 0.5 mol L⁻¹ H₂SO₄ solution over nanoparticles of Pt₅Ru₄Sn supported on carbon synthesized by colloidal method. The incorporation of the Ru and Sn to Pt facilitated the C–C bond cleavage, thus increasing the oxidative removal of CO and other carbonaceous species formed during the oxidation of ethylene glycol and glycerol. Structural and electronic modifications were observed in these catalysts, like changes in lattice parameter, as well as partial occupation of vacancies of *d* band of Pt.

Studies involving electro-activity of catalysts based on lead (Pb) are well known [25–30]. For instance, Casado-Rivera et al. [31] demonstrated that Pt–Pb catalysts are excellent candidates for using in direct formic acid fuel cell, exhibiting tolerance by CO poisoning.

The physicochemical properties and electro-activity of materials used as catalysts in fuel cells are related to several features such as: *i*) preparation method [14], *ii*) catalyst chemical composition [32,33], *iii*) particle size [34], *iv*) type and porosity of support [35,36] and, *v*) particles morphology [37,38], among others. For instance, the catalytic properties of Pt–M (M = Ru, Sn, Au, Pb) nanoparticles used in electrooxidation of liquid fuels are strongly affected by the synthesis route, i.e.: colloidal method [39], microwave-assisted thermal decomposition [40], electro-deposition [41], and sol-gel method [42].

Many alcohol oxidation studies have been done using bimetallic catalysts synthesized using several metals. Structures of Pt-based intermetallic and core–shell nanoparticles such as Pt/Sn are gaining attention due to their performance in many chemical and electrochemical reactions [43]. The development of binary catalysts with core–shell morphology (Au@Ni) for oxidation of glycerol in alkaline medium was proposed by Song et al. [44] and the main results indicate that these materials increase the electro-activity and decrease the sensitivity to CO poisoning, thus enabling their application to technological use in fuel cells.

To our knowledge, previous studies focusing on glycerol electrooxidation based on catalysts containing lead is scarcely found

in literature [45]. Due to high price of platinum, the development of high active electro-catalysts with low load of Pt is a major concern. In the present study, (Pb_x@Pt_y/C) CS electro-catalysts were investigated. These nanostructures were produced by successive reduction processes without using surfactants and tested for glycerol electrooxidation. Moreover, Pb_xPt_y/C alloy catalysts were also synthetized for comparison purposes. The catalysts were characterized by scanning transmission electron microscopy (STEM), high resolution transmission electron microscopy (HRTEM), X-ray powder diffraction (XRD), and X-ray photoelectron spectroscopy (XPS), while the electrocatalytic behavior of these materials for glycerol oxidation in acid medium was accessed by cyclic voltammetry, chronoamperometry and quasi-stationary potentiostatic polarization.

2. Experimental

2.1. Preparation of the catalysts

The Pb_x@Pt_y nanoparticles were prepared by dissolving the metal precursors, Lead chloride (PbCl₂, 98%, Aldrich) and hexachloroplatinic acid (H₂PtCl₆·6H₂O, 99.95%, Aldrich), with subsequent reduction in formic acid. The catalysts consisted of 20% (w/w) metal (Pb_x + Pt_y) on carbon with nominal x:y molar ratios of 1:3, 1:2, 1:1 and 2:1. The Pt/C was used as a reference sample. Initially, 0.0069 g of the PbCl₂ was dissolved in 10 mL of water and the formic acid (CH₂O₂, 98–100%, Vetec[®]) was slowly added under stirring by 1 hour. In this step the core solution was formed. Posteriorly, the H₂PtCl₆·6H₂O was dissolved in 15 ml of ultrapure water purified by a Milli-Q system from Millipore Inc. This solution was then added to the core solution with different ratios in order to prepare the CS catalysts with appropriate x:y molar ratios. Formic acid was again fed to solution as reducing agent to promote the formation of core–shell nanoparticles. This solution was continuously stirred until completely clear, assuring reduction of ions. The molar ratio between the precursor H₂PtCl₆·6H₂O and formic acid was the same used by Sun et al. [46], to reduce 6.18 × 10⁻⁵ mol of hexachloroplatinic acid, 2.65 × 10⁻² mol of formic acid was used. The carbon black (Alfa Aesar/Acetylene, 50% compressed, 99.9%, A Johnson Matthey Company) was added as support for Pb_x@Pt_y nanoparticles. The slurry was maintained under stirring by 24 h. Finally, the powder was washed with ultrapure water, recovered by filtration and dried at 70 °C. All chemicals were analytically pure. Pb_xPt_y/C alloys were also synthesized using the same Pb and Pt proportions of core–shell nanoparticles for comparative purposes. For the preparation of Pb_xPt_y/C alloy catalysts, a similar procedure was adopted. The difference is related to addition of precursors, which was realized in a single step.

2.2. Physical characterizations

The crystal structure was determined by X-ray diffraction in a Rigaku diffractometer model RINT ULTIMA + UNIVERSAL 2000/PC, using CuK α radiation ($\lambda = 0.15406$ nm). The diffractograms were registered between 2 θ angles from 20 to 90°, with a scan rate of 2° per minute. The working conditions of the powder diffractometer were 1600 KW, a tension of 40 KV and a current of 40 mA.

Transmission electron microscopy images were obtained using a JEOL (JEM 2100HTP) microscope at 200 kV. A few droplets of an ultrasonically dispersed suspension of each catalyst in ethanol were placed on a copper grid with lacey carbon film and dried at ambient conditions for TEM characterizations. Particle size distributions were constructed by using about 320 particles for each catalyst.

Scanning transmission electron microscopy (STEM) analyses were performed using a FEI-Tecnai G² F20 microscope operating

at 200 kV, equipped with a high angle annular dark field (HAADF) and energy dispersive X-ray (EDX) detectors.

XPS characterization was carried out in a VG-Microtech Multilab 3000 electron spectrometer using Mg-K α (1253.6 eV) radiation source. To obtain the XPS spectra, the pressure of the analysis chamber was maintained at 5×10^{-10} mbar. The binding energy (BE) scale was adjusted by setting the C1s transition at 284.6 eV.

2.3. Electrochemical measurements

Electrochemical measurements were performed and recorded at room temperature using an Autolab Model PGSTAT 302 N potentiostat/galvanostat (Eco Chemie B.V, Holland). Experiments were carried out in a glass cell (one compartment) using a conventional three-electrode set up (half-cell). Boron-doped diamond (BDD) electrodes were used as substrates for the electrocatalytic material [27,47], which were prepared in the *Centre Suisse d'Electronique et de Microtechnique* SA (CSEM), Neuchâtel. The boron content was about 800 ppm and the geometrical area of the working electrode exposed to the solution was 0.54 cm^2 . The reference system used was a hydrogen electrode in the same solution (HESS) connected by a Luggin capillary, and a Pt coil (1 cm^2) was used as counter electrode. All potentials are referred to the reversible hydrogen electrode (RHE). Nitrogen gas was bubbled in all solutions for 15 min before starting each electrochemical test. The catalyst 'ink' was prepared using 0.008 g of suspension powder catalyst in 1 mL of ultrapure water (purified by Milli-Q system) and 200 μL Nafion® solution (5 wt.% Aldrich solution), which was dispersed in an ultrasonic bath (Ultra Cleaner Unique/1450A). Then, 0.06 cm^3 catalyst suspension was transferred with an injector to a BDD electrode. Resulting in a metal charge, on the working electrode, of 2.59 mg cm^{-2} . Finally, the electrode was heated at 60°C for 20 min.

Electrochemical activity tests were performed in aqueous 0.5 mol L^{-1} H_2SO_4 solutions containing 0.5 mol L^{-1} $\text{C}_3\text{H}_8\text{O}_3$ at room temperature. Cyclic voltammetry experiments were performed between 0.05 and 0.80 V until stationary responses were obtained, then two voltammetric cycles were performed between 0.05 and 1.30 V at a scan rate of 0.02 V s^{-1} to evaluate the behavior of each electrocatalyst. Chronoamperometric experiments were performed at 0.60 V for 600 s, and anode polarization curves obtained between 0.1 and 0.8 V in the potentiostatic mode, with all data points obtained after 300 s of polarization at each potential. The stability of the anode electro-catalyst synthesized by chemical reduction method was evaluated by cycling the electrode potential between 0.05 and 1.30 V versus RHE for 3000 cycles. The electrochemical active surface (EAS) areas of the catalysts were estimated supposing that the normalized charge density for a monolayer of adsorbed carbon monoxide on polycrystalline Pt is $420 \mu\text{C cm}^{-2}$. Afterwards, the normalized EAS was obtained with respect to the Pt mass contained in the electrode surface for each catalyst.

CO-stripping voltammetry was performed between 0.05 and 0.8 V after the electrode was cleaned with 30CV cycles. While the potential was held at 0.1 V , the electrolyte solution was purged with a 5% CO/95% Ar gas mixture for 10 min. After 10 min, the solution was purged with N_2 for 25 min to remove trace CO not adsorbed on the catalyst. Then the potential was scanned from 0.05 up to 1.3 V at 20 mV s^{-1} . After the CO-stripping voltammetry, another CV scan was conducted to ensure complete removal of CO from the solution. In order to compare the intrinsic activities of different catalysts, the currents obtained from the electrochemical half-cell experiments were normalized per total surface active area obtained by stripping of a monolayer of CO and considering a charge of $420 \mu\text{C cm}^{-2}$ [48,49].

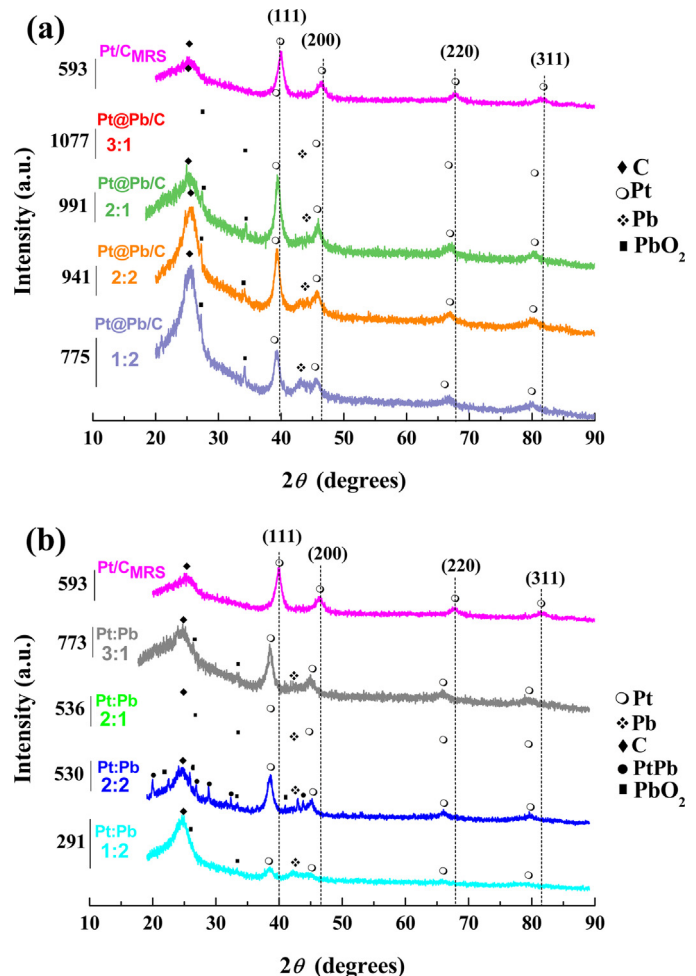


Fig. 1. XRD patterns taken for the Pt/C electrocatalyst, and for the electrocatalysts containing Pb and Pt (Pb:Pt) with different molar ratios: 1:3, 1:2, 1:1 and 2:1, respectively. (a) core-shell electrocatalysts (b) alloy electrocatalysts. The values shown in the y axis correspond to the values of the peak related to the Pt (111) crystal lattice and vertical lines correspond to the 2θ positions of pure polycrystalline Pt.

3. Results and discussion

3.1. Catalysts Characterization

The X-ray powder diffraction patterns of the $\text{Pb}_x\text{Pt}_y/\text{C}$ and $\text{Pb}_x\text{Pt}_y/\text{C}$ catalysts are shown in Fig. 1(a) and (b), respectively. All the X-ray diffractograms present a broad peak at about 25° , assigned to the (002) plane of the graphite-like crystalline structure of the carbon support (JCPDS N° 00-001-0640) and four diffraction peaks assigned to the Pt (111), (200), (220) and (311) planes, respectively, which represent the typical feature of the face centered cubic (fcc) polycrystalline Pt. Moreover, a small peak can be observed at $\sim 43^\circ$ which could correspond to the (110) diffraction plane of Pb (JCPDS N° 00-044-0872). In addition, Pb was also deposited as PbO_2 (JCPDS N° 00-037-0517). The displacement of Pt peaks to lower angles may be related to the insertion of Pb into the Pt crystal structure (alloying) during the synthesis, forming a Pb_xPt_y solid solution into the nanoparticle shell, as previously reported in Pt core-shell nanoparticles [50,51].

The equilibrium phase diagram of the Pb–Pt system does not predict the formation of Pb–Pt solid solution been the formation of intermetallic compounds thermodynamically favorable [52]. On the other hand, the formation of a metastable solid solution at the Pb/Pt interface during the synthesis of the core–shell nanoparticles cannot be disregarded. Moreover, it is also possible to have an

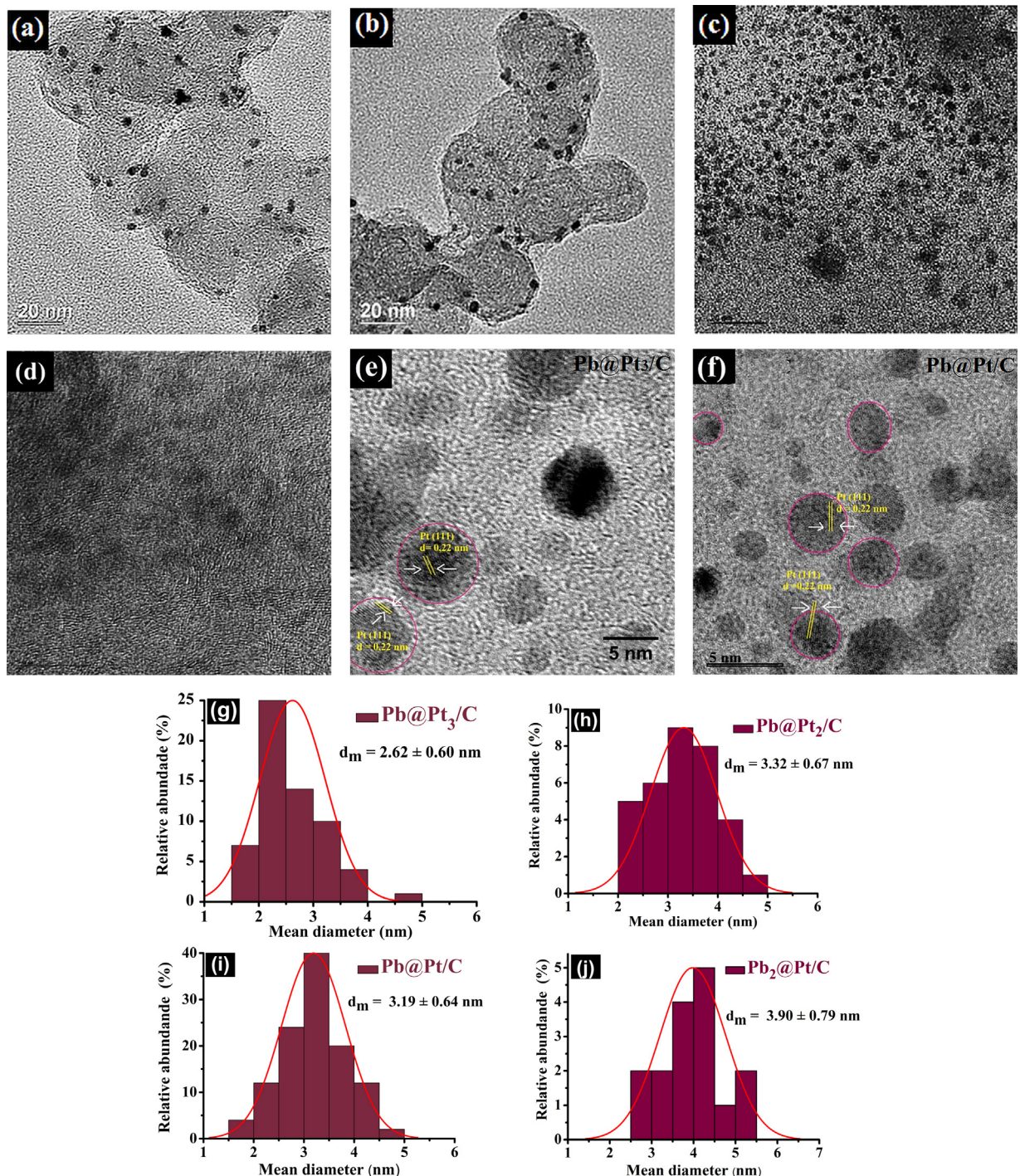


Fig. 2. Transmission electron microscopy images of $\text{Pb}_x@\text{Pt}_y/\text{C}$ electrocatalysts: (a) $\text{Pb}@\text{Pt}_3/\text{C}$; (b) $\text{Pb}@\text{Pt}_2/\text{C}$; (c) $\text{Pb}@\text{Pt}/\text{C}$; (d) $\text{Pb}_2@\text{Pt}/\text{C}$; (e and f) are micrographs with higher magnification taken for $\text{Pb}@\text{Pt}_3/\text{C}$ and $\text{Pb}@\text{Pt}/\text{C}$ catalysts; (g, h, i, j) are the histograms of the average diameter distribution of particle catalysts $\text{Pb}_x@\text{Pt}_y/\text{C}$ in 0–5 nm size range.

expansion of the Pt lattice parameter due to stress on the Pt shell promoted by the nucleus of Pb which has a larger lattice parameter. The Pt lattice parameters for $\text{Pb}@\text{Pt}_3/\text{C}$, $\text{Pb}@\text{Pt}_2/\text{C}$, $\text{Pb}@\text{Pt}/\text{C}$ e $\text{Pb}_2@\text{Pt}/\text{C}$, calculated from the XRD patterns, changed from 0.3910 nm for Pt/C catalyst to 0.3959 nm, 0.3953 nm, 0.3960 nm, and 0.3961 nm, respectively. The thickness of the Pt (220) peak was used to estimate the average crystallite size according to the Scherrer's equation. The $\text{Pb}@\text{Pt}_3/\text{C}$, $\text{Pb}@\text{Pt}_2/\text{C}$, $\text{Pb}@\text{Pt}/\text{C}$ and $\text{Pb}_2@\text{Pt}/\text{C}$ samples had their average crystallite sizes estimated as 2.104 nm, 2.153 nm, 2.378 nm, 2.214 nm and 2.692 nm, respectively.

The diffraction peaks of the $\text{Pb}_x\text{Pt}_y/\text{C}$ catalysts (Fig. 1(b)) are shifted to lower 2θ values with respect to the position of the Pt/C peaks. These results suggest the incorporation of Pb into the Pt crystal structure in accordance with results presented by Buzzo et al. [42] and Youn et al. [53] for Pt–Pb alloys. The shift in diffraction angles was more pronounced for Pb_xPt_y alloys than for $\text{Pb}_x@\text{Pt}_y/\text{C}$ catalysts, indicating a more extensive alloy formation for the first samples, as expected [42,53]. The values of average particle sizes and lattice parameters are presented in Table S1 of the Supporting Information. These values are similar for all the core–shell electrocatalysts presenting observable variations for alloy nanoparticles.

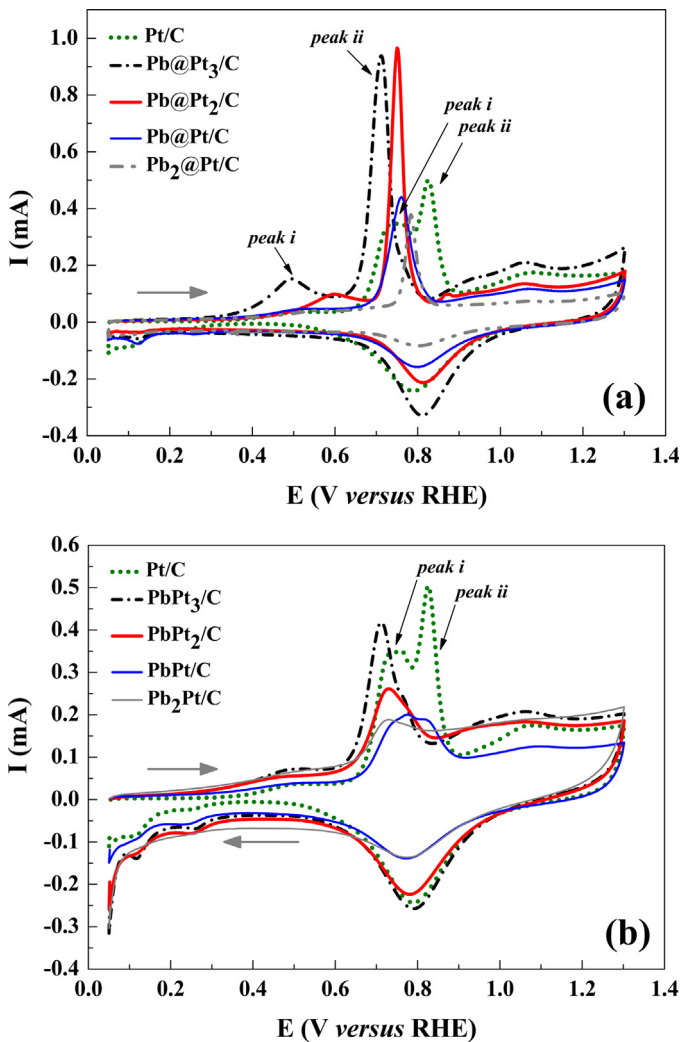


Fig. 3. CO stripping curves for the $\text{Pb}_x\text{@Pt}_y\text{/C}$: (a) $\text{Pb@Pt}_3\text{/C}$; $\text{Pb@Pt}_2\text{/C}$; Pb@Pt/C ; $\text{Pb}_2\text{@Pt/C}$ and Pt/C ; and $\text{Pb}_x\text{Pt}_y\text{/C}$; (b) $\text{PbPt}_3\text{/C}$; $\text{PbPt}_2\text{/C}$; PbPt/C ; $\text{Pb}_2\text{Pt/C}$ and Pt/C in a $0.5 \text{ mol L}^{-1} \text{ H}_2\text{SO}_4$ solution, $v = 20 \text{ mV s}^{-1}$.

Bright field TEM images and particle size histograms of the $\text{Pb}_x\text{@Pt}_y\text{/C}$ catalysts are shown in Fig. 2(a–f) and (g–j), respectively. Well-dispersed $\text{Pb}_x\text{@Pt}_y$ nanoparticles on the carbon support can be observed for all the samples. The average sizes of the nanoparticles obtained from TEM results (Fig. 2(g–j) and data in Table S1 of the Supporting Information) agree well with values calculated from XRD patterns. The average particles size obtained for $\text{Pb}_x\text{@Pt}_y\text{/C}$ catalysts are found in the same range reported by Shimizu et al. [54] and Lima et al. [55]. In Fig. 2(e) and (f), high resolution TEM micrographs for $\text{Pb@Pt}_3\text{/C}$ and Pb@Pt/C are presented. From the micrographs obtained for the $\text{Pb@Pt}_3\text{/C}$ and Pb@Pt/C electrocatalysts in a 5 nm scale, 0.22 nm gaps were seen between the adjacent planes, different from what was seen for the planes (111) of Pt, around 0.23 nm [56]. This stress imposed to the Pt structure can be due to the local geometrical defects related to superficial tension [57].

3.2. Electrochemical Characterization

CO stripping curves of the studied catalysts are presented in Fig. 3(a) and (b). In Fig. 3(a), it is possible to see the dislocation of CO oxidation potential of the core-shell catalyst to lower values than pure Pt. Similarly seen in Fig. 3(b) for alloys. Besides, a reduction in current with lower amounts of Pt in the catalyst for the Pt/Pb

compositions is probably attributed to a lower active area of these materials, which propitiates a lower amount of active sites for CO adsorption and oxidation.

The normalized EAS areas were estimated using the charging current obtained from the CO oxidation peaks. The normalized EAS values for $\text{Pb@Pt}_3\text{/C}$ and Pt/C are $267.3 \text{ m}^2 \text{ g}_{\text{Pt}}^{-1}$ and $143.5 \text{ m}^2 \text{ g}_{\text{Pt}}^{-1}$, respectively; thus revealing that a higher amount of exposed active sites of Pt is indeed available for the core-shell structure than on pure Pt/C catalytic composite, suggesting an improved Pt utilization. An increase of the normalized EAS area is observed by increasing the Pt content in the $\text{Pb}_x\text{@Pt}_y\text{/C}$ catalysts. The normalized EAS area values are 144.0 , 160.0 and $183.2 \text{ m}^2 \text{ g}_{\text{Pt}}^{-1}$ for $\text{Pb@Pt}_2\text{/C}$, Pb@Pt/C and $\text{Pb}_2\text{@Pt/C}$, respectively. The normalized EAS values for the $\text{PbPt}_3\text{/C}$, $\text{PbPt}_2\text{/C}$, PbPt/C and $\text{Pb}_2\text{Pt/C}$ alloys were 142.0 , 118.7 , 105.7 and $84.8 \text{ m}^2 \text{ g}_{\text{Pt}}^{-1}$, respectively. The areas of the electrocatalysts with 1:3, 1:2, 1:1 and 2:1 ratios presented values close to the values found in the core-shell structures of the same compositions.

The CO oxidation peak potential of the Pt/C catalyst found in Fig. 3(a) is in agreement with data found in literature [58,59]. Although the CO oxidation onset potential at the Pt/C (dot curve) is around 0.74 V (peak “i”), the predominant peak occurred on $\sim 0.82 \text{ V}$ (peak “ii”). Similar behaviour for $\text{Pb@Pt}_3\text{/C}$, presenting the formation of two oxidation peaks with potential of CO on $\sim 0.5 \text{ V}$ (peak “i”) and on $\sim 0.71 \text{ V}$ (dash dot curve), is seen. The existence of two peaks in Pt nanoparticles was already observed by other researchers [60,61].

The $\text{Pb@Pt}_3\text{/C}$ core-shell nanostructure shows a negative potential shifting (of $\sim 110 \text{ mV}$) for CO-stripping compared to pure Pt. It demonstrates that the alcohol is oxidized to CO at lower potentials, as well as it indicates that the core-shell catalyst oxidized the adsorbed CO to CO_2 at lower potentials than pure Pt. This behaviour indicates that the interaction between the atoms of the Pb core and the shell rich in Pt leads to a weakening of the adsorption force of Pt–CO onto the catalyst surface [62,63], thus resulting in a CO-stripping at $\sim 0.71 \text{ V}$ (peak “ii”) for $\text{Pb@Pt}_3\text{/C}$.

Fig. 4(a) shows the cyclic voltammograms obtained in the $0.5 \text{ mol L}^{-1} \text{ H}_2\text{SO}_4$ electrolyte at a scan rate of 0.02 V/s for $\text{Pb}_x\text{@Pt}_y\text{/C}$ catalysts, presenting the typical regions associated with adsorption/desorption processes of H_{upd} ($\text{H}^+ + \text{e}^- = \text{H}_{\text{upd}}$). The $\text{Pb@Pt}_3\text{/C}$ electro-catalyst exhibits the typical behavior regarding the hydrogen and the oxide regions of Pt in the materials in acid solutions for Pt nanoparticles on the surface. According to results reported in the literature, peaks with good definition on H_{upd} region are attributed to desorption of hydrogen coming from Pt nanoparticles with low average sizes. Average size of nanoparticles is 2.62 nm (determined by TEM). In Fig. 4(a), a marked reduction in oxygen species (0.75 – 1.00 V) for $\text{Pb@Pt}_3\text{/C}$ catalysts can be observed, indicating that the oxygen species at the surface of the nanoparticles (Pt–OH, Pt–O and Pt–O₂) have weaker adsorption energies (ΔG_{ads}) than those observed in pure Pt catalyst. Moreover, this is an indicative of an easier desorption of oxygen species [64,65]. However, the weaker adsorption of hydroxyls species could increasing the turnover frequency of the catalysts (the amount of electrons transferred per unit surface area per unit time). Therefore the catalytic active sites on surface of nanoparticles will be more quickly available for further oxidation glycerol molecules, increasing the fuel cell efficiency.

The low definition adsorption/desorption peaks for the $\text{Pb}_2\text{@Pt/C}$ are related to high content of Pb (66.6 wt%) compared with other electro-catalysts. This amount can cause because the low content of Pt may not cover the Pb particles [66]. Theoretically, for a full coverage of a Pb nanoparticle of 2 nm (atomic radius = 1.54 \AA) containing 6.4935 atoms composing the core, is necessary 14.388 Pt atoms (atomic radius = 1.39 \AA) to produce a coating which can fully cover the Pb core. Thus, it takes 2.2 times Pt atoms to cover a core of Pb. In the case of the $\text{Pb@Pt}_3\text{/C}$ catalyst, the atomic Pt con-

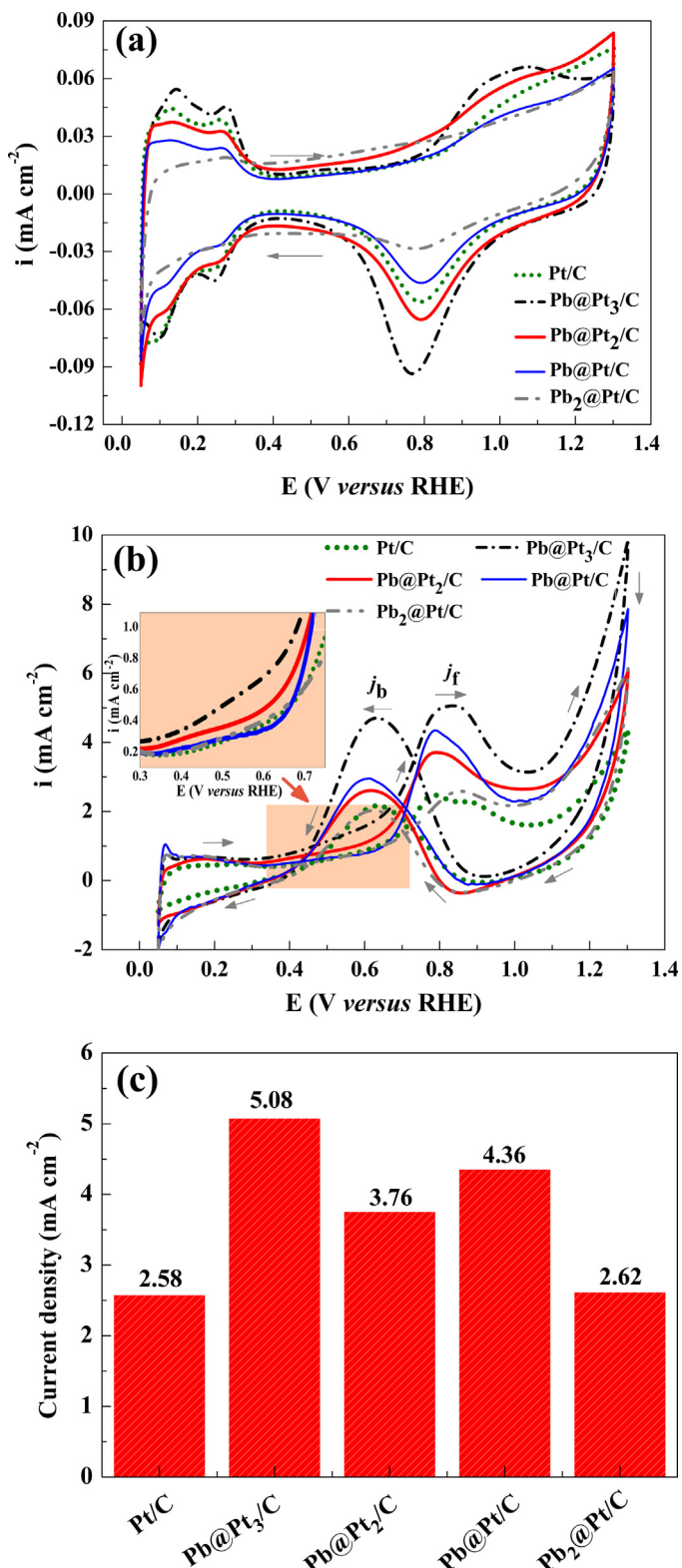


Fig. 4. (a) Cyclic voltammograms of $\text{Pb}_x\text{@Pt}_y\text{/C}$ and Pt/C catalysts in $0.5 \text{ mol L}^{-1} \text{H}_2\text{SO}_4$. (b) cyclic voltammograms of glycerol oxidation reaction on catalysts $\text{Pb@Pt}_3\text{/C}$, $\text{Pb@Pt}_2\text{/C}$, Pb@Pt/C , $\text{Pb}_2\text{@Pt/C}$ and Pt/C taken in $0.5 \text{ mol L}^{-1} \text{H}_2\text{SO}_4 + 0.5 \text{ mol L}^{-1}$ glycerol solutions. $v = 20 \text{ mV s}^{-1}$. The inset in (b) indicates the beginning of glycerol oxidation for each catalyst. (c) Comparative plotting the pseudo-current density peaks for glycerol oxidation in the forward scan for all the tested catalysts.

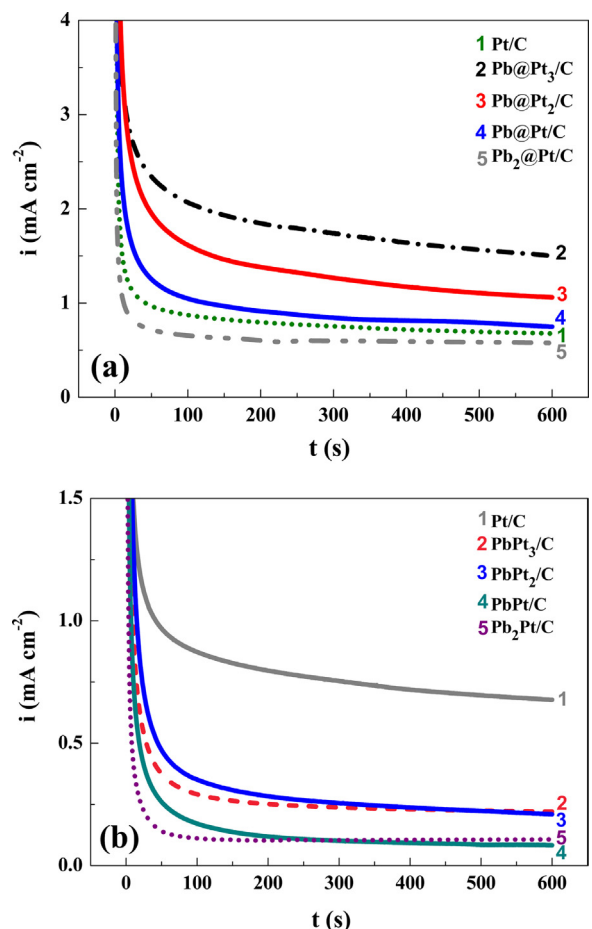


Fig. 5. Chronoamperometric curves of the (a) $\text{Pb}_x\text{@Pt}_y\text{/C}$ electrocatalysts compared to Pt/C and (b) $\text{Pb}_x\text{Pt}_y\text{/C}$ alloy electrocatalysts compared to Pt/C in $0.5 \text{ mol L}^{-1} \text{H}_2\text{SO}_4 + 0.5 \text{ mol L}^{-1}$ glycerol (applying 600 mV for 600 s).

tent is three times higher than Pb, considering that all Pt ions were reduced during the synthesis. This Pt content should be enough for ensuring the formation of a fully covered core (Pb) – shell (Pt) nanostructure.

Fig. 4(b) shows the curves of cyclic voltammetry typical for the glycerol electrooxidation reaction, with two anodic current peaks in positive and negative sweeps, respectively, which are related to the oxidation reaction of glycerol in the positive sweep and the incomplete oxidized carbonaceous residues on the catalyst surface during the negative sweep [3,67]. In Fig. 4(b), the major current density of oxidation (5.08 mA cm^{-2}) is observed for $\text{Pb@Pt}_3\text{/C}$ catalyst during anodic sweeps. In contrast, a drop of these values of 3.76 , 4.36 , 2.62 and 2.58 mA cm^{-2} is obtained for $\text{Pb@Pt}_2\text{/C}$, Pb@Pt/C , $\text{Pb}_2\text{@Pt/C}$ and Pt/C electro-catalysts (see, Fig. 4(c)) with the increase in the Pb content in the catalyst.

Roquet et al. [68] established that glycerol oxidation in acid media in Pt electrode produces glyceraldehyde, glycol acid and formic acid as (reaction 1) intermediates of reaction. Koper et al. [69] studied the glycerol oxidation on Pt catalysts in $0.01 \text{ mol L}^{-1} \text{HClO}_4$ and identified species containing two carbons (as glycolic acid) and one carbon (as formic acid) by using *in situ* FTIR measurements. Similarly, Gomes and Tremilliosi-Filho [70], by using *in situ* FTIR, showed that tartronic acid, glyceric acid, glycolic acid and formic acid are formed from the glycerol oxidation on Pt in $0.1 \text{ mol L}^{-1} \text{H}_2\text{SO}_4$ at 1.2 V .

The formic acid formed during glycerol electrooxidation can form CO_{ads} species [69] on electrode surface (see, reaction 2) [17]. Otherwise, it was shown, by using *in situ* FTIR and isotopi-

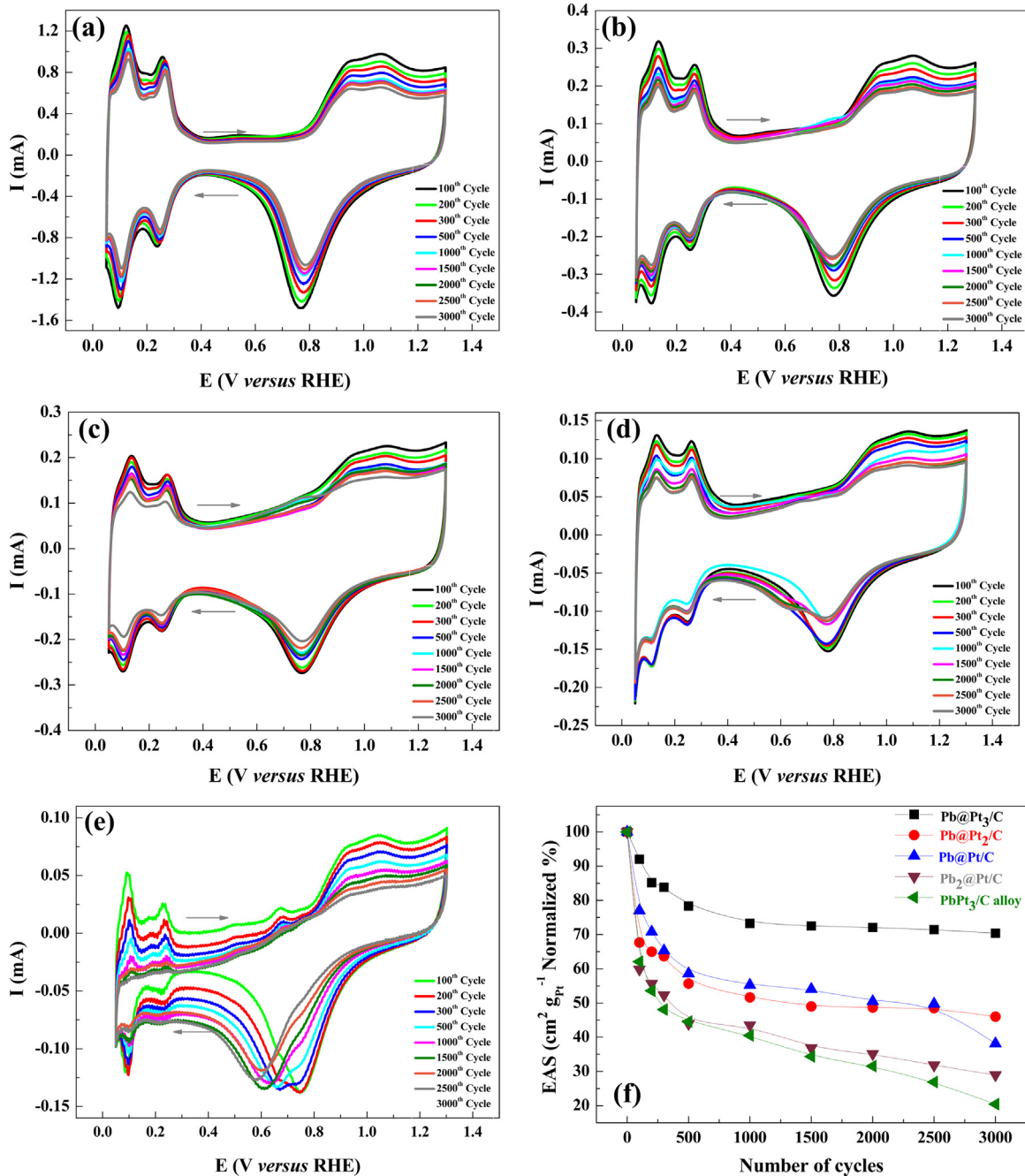
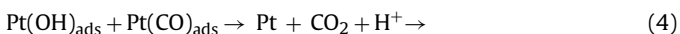


Fig. 6. Electrochemical stability accessed by cyclic voltammetry of catalysts (a) Pb@Pt₃/C, (b) Pb@Pt₂/C, (c) Pb@Pt/C, (d) Pb₂@Pt/C and (e) PbPt₃/C (alloy); (f) EAS $\text{cm}^2 \text{g}_{\text{Pt}}^{-1}$, normalized by the initial EAS (in percentage) as a function of the number of cycles, with a total cycling time of 15 hours in 0.5 mol L⁻¹ H₂SO₄, $v = 100 \text{ mV s}^{-1}$.

cally labeled glycerol (¹³CH₂OH–¹²CHOH–¹³CH₂OH), that terminal (¹³CH₂OH) and central (¹²CHOH) groups, from cleaved glycerol molecules, are able to form adsorbed CO_{ads} accumulated on the Pt surface (for a Pt/C catalyst) in 0.1 mol L⁻¹ HClO₄ medium [71]. Thus, the only way to remove CO is oxidizing it to CO₂ by reacting with OH_{ads} species formed by the dissociation of water molecules on the Pt surface (reaction 3 and 4).



However, the water activation process on Pt is very difficult and occurs at high potential (> 0.5 V). Due to the higher potential of CO oxidation on Pt, the electrode surface will be blocked by the further amount CO species generated, thereby hindering the adsorption of other glycerol molecules on the electrode surface [72]. This results in the oxidation of a reduced number of glycerol moieties. Therefore, the high glycerol oxidation current depends mainly on the amount of CO oxidized and removed from the active sites of Pt at lower potentials. Thus, it is suggested that the smaller pseudo-current density peaks found for the catalysts Pb@Pt₂/C, Pb@Pt/C, Pb₂@Pt/C and Pt/C are related to accumulation “CO” at Pt sites; thus decreasing the activity of the material. The process expressed by reaction 5 shows the dissociative adsorption

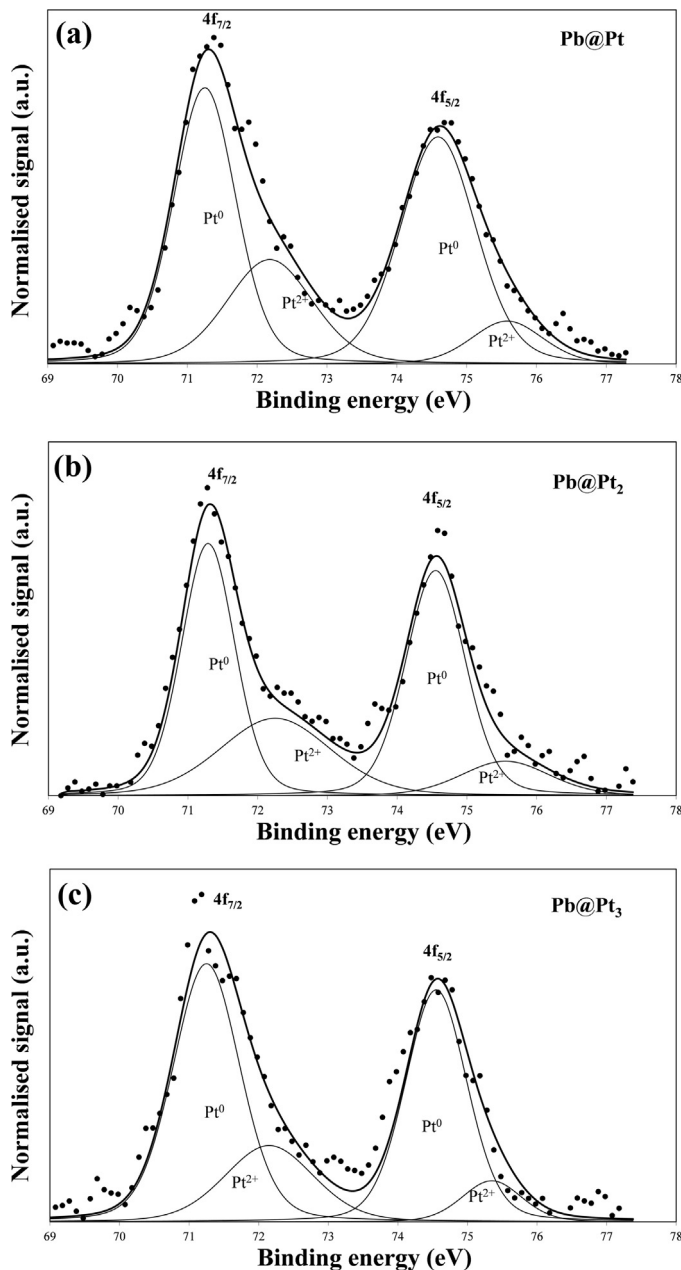
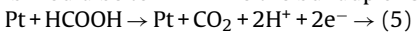


Fig. 7. Pt 4f transition in XPS experiments performed with core-shell catalysts.

of HCOOH that occurs on the surface of Pt. In this case, the function of Pb would be to minimize the buildup of CO at the Pt sites.



The E_i values (determined using a current density of 0.3 mA cm^{-2}), which is the onset of the glycerol oxidation are 0.43 V for $\text{Pb}@\text{Pt}_2/\text{C}$ and 0.52 V for $\text{Pb}@\text{Pt}/\text{C}$, $\text{Pb}_2@\text{Pt}/\text{C}$ and Pt/C electro-catalysts. For $\text{Pb}@\text{Pt}_3/\text{C}$ electro-catalyst, the glycerol molecules are adsorbed on electrode surface at potential lower than 0.36 V , and from this point the current starts to increase. This value is lower than that reported by Grace and Pandian [17], which was 0.50 V during glycerol oxidation using Pt–Pd alloy catalyst.

The results of catalytic activity obtained for $\text{Pb}@\text{Pt}_3/\text{C}$ electro-catalysts can be attributed to structural [54,63] and electronics effects [73,74,75,76]. The density energy of d -band of electronic states of Pt is displaced to low values in core–shell nanoparticles, inducing alterations correlated with quimisorption energy [77]. On the other hand, the modification induces by Pb into Pt electronic

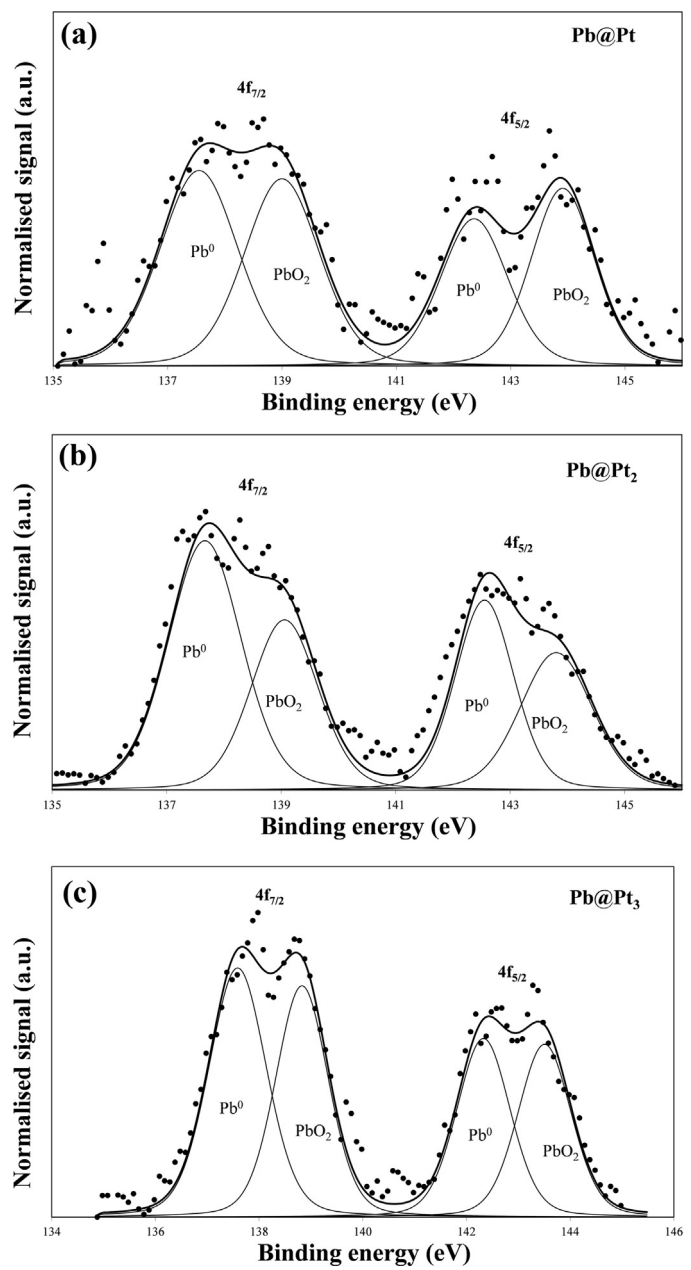


Fig. 8. Pb 4f transition in XPS experiments performed with core-shell catalysts.

structure (increase in the d -band vacancies of Pt) may raise the active sites for alcohol adsorption. Kaplan et al. [78] explained that the presence of a second metal as core results in a weakening of Pt–CO bonds. Similarly, Mott et al. [79] have related a synergistic effect in the activity of Pt–Au nanoparticles with elimination of poisoners species adsorbed on the surface and the change in level of d -band resulting in changes in surface adsorption force.

Considering that the electron transfer process of superficial reaction occurs proportionally to the number of electrons transferred per unit of area and time, chronoamperometry measurements were performed at 0.60 V for $\text{Pb}_x@\text{Pt}_y/\text{C}$ (Fig. 5(a)), $\text{Pb}_x\text{Pt}_y/\text{C}$ (Fig. 5(b)) and Pt/C samples to compare the catalytic activity of the anode catalysts. In Fig. 5, after applying a potential, there was a sharp decrease in the current density due to the charging of the double-layer and others surface processes at the electrode [80]. In Fig. 5(a), the values of equilibrium current densities (i_{eq}) were 1.50 mA cm^{-2} , 1.04 mA cm^{-2} , 0.77 mA cm^{-2} , 0.60 mA cm^{-2}

and 0.71 mA cm^{-2} , for $\text{Pb}@\text{Pt}_3/\text{C}$, $\text{Pb}@\text{Pt}_2/\text{C}$, $\text{Pb}@\text{Pt}/\text{C}$, $\text{Pb}_2@\text{Pt}/\text{C}$ and Pt/C , respectively. The catalyst with core–shell structure, $\text{Pb}@\text{Pt}_3/\text{C}$, displays the highest pseudo-current density in comparison with other compositions (the value was 2.11 times higher than that of Pt/C).

Chronoamperometry measurements were used for the comparative study of $\text{Pb}_x\text{Pt}_y/\text{C}$ alloy and $\text{Pb}@\text{Pt}_3/\text{C}$ nanostructures. It was observed from Fig. 5(b), the decay of pseudo current density for an equilibrium state occurs after about 2 min for $\text{Pb}_x\text{Pt}_y/\text{C}$ electro-catalysts. This decay is followed by a quasi-stationary-state for all samples. The PbPt_3/C , PbPt_2/C , PbPt/C and $\text{Pb}_2\text{Pt}/\text{C}$ electro-catalysts showed lower values of i_{eq} : 0.24 mA cm^{-2} , 0.20 mA cm^{-2} , 0.09 mA cm^{-2} and 0.11 mA cm^{-2} , respectively, compared with the $\text{Pb}_x@\text{Pt}_y/\text{C}$ catalyst. The values of i_{eq} for $\text{Pb}@\text{Pt}_3/\text{C}$, $\text{Pb}@\text{Pt}_2/\text{C}$, $\text{Pb}@\text{Pt}/\text{C}$ core–shell samples were 6.25, 5.20 and 8.75 times higher than the observed for PbPt_3/C , PbPt_2/C and PbPt/C alloys samples synthesized in the same compositions.

The stability of the anode electro-catalyst synthetized was evaluated by cycling the electrode potential between 0.05 and 1.30 V versus RHE for 3000 cycles. Fig. 6 shows the electrochemical stability of $\text{Pb}@\text{Pt}_3/\text{C}$, $\text{Pb}@\text{Pt}_2/\text{C}$, $\text{Pb}@\text{Pt}/\text{C}$ and $\text{Pb}_2@\text{Pt}/\text{C}$, as well as, the EAS area values normalized by the initial EAS (taken in the second cycle) determined for each catalyst (in percentage) as a function of the number of potential cycles. The normalized EAS area for $\text{Pb}@\text{Pt}_3/\text{C}$ shows the best stability compared with other catalysts.

The $\text{Pb}@\text{Pt}_3/\text{C}$ electro-catalysts present stabilization after 1000 cycles, which is not observed in other core–shell catalysts and PbPt_3/C alloy. The $\text{Pb}@\text{Pt}_3/\text{C}$ catalyst reached the stability after 1500 cycles. This behavior can be attributed to major amount of Pt at the surface. Conversely, for $\text{Pb}@\text{Pt}_2/\text{C}$, $\text{Pb}@\text{Pt}/\text{C}$ and $\text{Pb}_2@\text{Pt}/\text{C}$ a possible dissolution process may occur due to appearance of characteristic peak of Pb [28,81] at potentials of 0.6–0.8 versus RHE during anodic sweep. This peak is clearly observed for PbPt_3/C alloy catalyst.

The surface valence states of Pb and Pt in $\text{Pb}_x@\text{Pt}_y/\text{C}$ catalysts were determined by XPS analyses, presented in Figs. 7 and 8. XPS analysis provided information about catalyst surface compositions. The signals were treated with the XPSPEAK41 program using a sum of Lorentzian–Gaussian functions. The C1s signal (284.6 eV) was used as reference.

The Pt 4f signal, Fig. 7, shows two signals deconvoluted in two peaks of the $4f_{7/2}$ and $4f_{5/2}$. The peaks have the maxima around at 71.2, 72.1, 74.5 and 75.5 eV, which allow identifying different oxidation states of Pt. The more intense doublet belongs to Pt^{00} and the weaker one is assigned to Pt^{2+} species, such as PtO and $\text{Pt}(\text{OH})_2$ [82,83].

Fig. 8 shows the Pb 4f region of the XPS spectra and it is also resolved into two components ($4f_{7/2}$ and $4f_{5/2}$ states). These broad profiles were also deconvoluted into four different peaks, which allow identifying the different oxidation states of Pb. The peaks approximately at 137.5 and 142.3 eV are attributed to Pb^0 and the others two peaks, around at 139.0 and 143.5 eV are correlated with Pb^{4+} species. Although the four peaks are almost same size, the fitting Pb spectra indicate major proportion of non-oxidized Pb species [84] (see, Table S2 in the Supporting Information).

The oxygen spectra were also obtained by XPS and presented in Fig. 9. The fraction of each surface oxygen groups was obtained by deconvolution of the O 1s peak in three components, namely, carbonyl oxygen (peak at 531.8 eV), oxygen atoms in $\text{C}=\text{O}$ bonds, like hydroxyl and ether groups (peak at 533 eV) and oxygen atoms in acidic carboxyl groups (peak at 534 eV). The Table S3 (Supporting Information) shows the percentage of the different oxygen species, the hydroxyl and carboxyl groups are the majority of the three components. These result is in accord with the presence of PtO and $\text{Pt}(\text{OH})_2$ species [85].

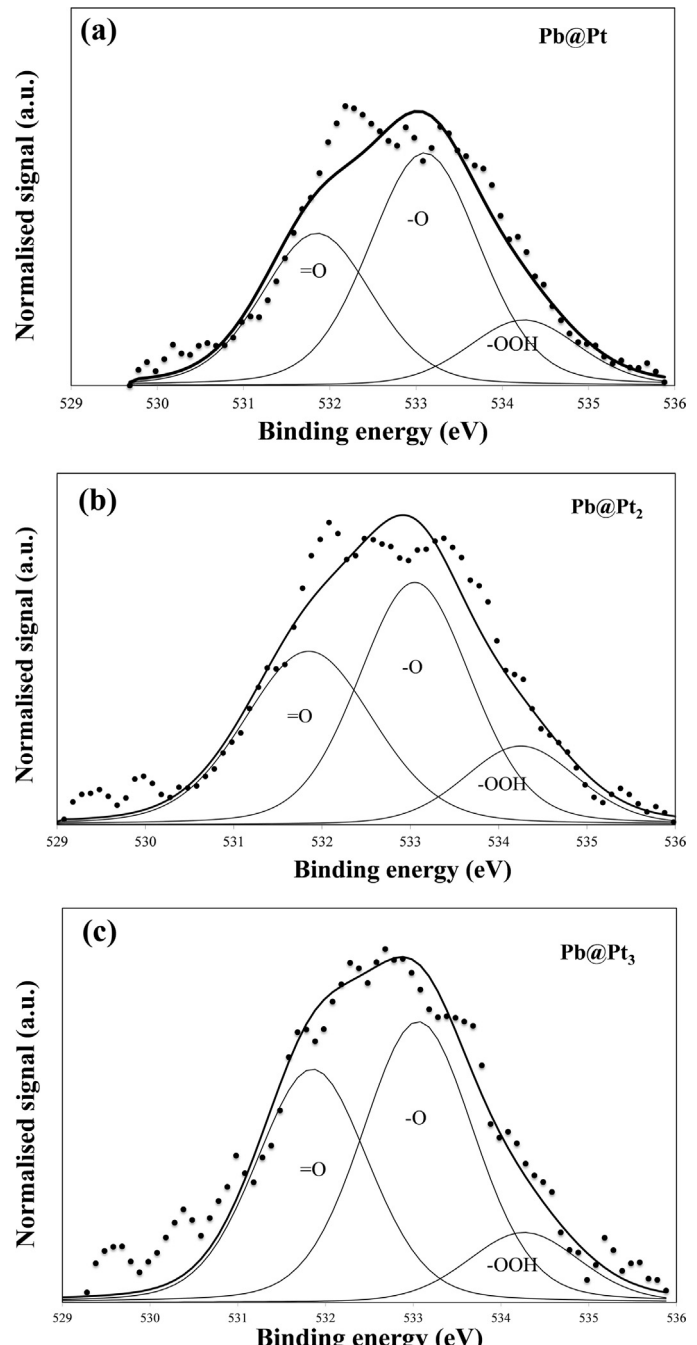


Fig. 9. O 1s transition in XPS experiments performed with core–shell catalysts.

The fractions of Pb and Pt species calculated from the relative intensities of deconvoluted and Pb/Pt surface composition observed from the XPS results are summarized in Table S2 in the Supporting Information. It is found that Pt^0 is a predominant species in $\text{Pb}@\text{Pt}_2/\text{C}$ and $\text{Pb}@\text{Pt}/\text{C}$ (82 and 88%, respectively) with small amounts of the oxidized Pt species (18 and 12%). It is found that Pt^0 is a predominant species in all the samples with smaller amounts of the oxidized Pt species. The surface Pt/Pb atomic ratio indicates a clear enrichment of Pt in the outermost layers by segregation of Pt onto the surface. Finally, it was concluded that in general, the interaction between both metals in the CS structure led to an effective alteration of the surface atom electron densities that, in its turn, should influence their activity characteristics.

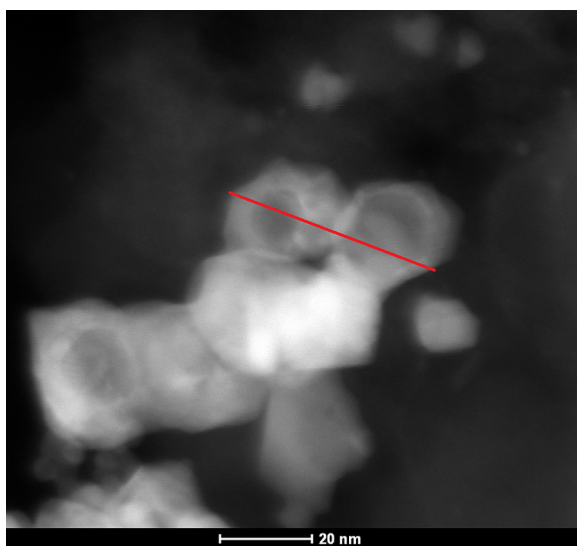


Fig. 10. HAADF-STEM image of a small agglomerate of $\text{Pb}@\text{Pt}_3/\text{C}$ core–shell nanoparticles. The line crossing two adjacent nanoparticles indicates where the EDX line scan was performed Pb.

Fig. 10 shows the HAADF-STEM image of the $\text{Pb}@\text{Pt}_3/\text{C}$ sample, which showed the most interesting electrochemical properties (as referred in the following section) among the investigated materials. The incoherent image obtained through the HAADF detector has a strong contrast related to the atomic number. Therefore, HAADF images are sensitive to the chemical composition of the nanoparticles [86]. In **Fig. 10** a small agglomerate of few nanoparticles is observed. For the $\text{Pb}@\text{Pt}_3/\text{C}$ core–shell nanoparticles, it might be expected a more intense HAADF signal (brighter contrast) for lead (core element) since it has higher atomic number than Pt. This feature is observed for the nanoparticle in the center of the agglomerate. Conversely, other particles show exactly the opposite behavior with dark contrast in the core. This feature may be associated to the oxidation of Pb during the core synthesis, leading to a nucleus with lower density of Pb and, consequently, lower electronic density than the expected. This result agrees well with the observed Pb oxide peaks in XRD and oxidized state of Pb determined by XPS analyzes. The EDX line-scan spectra for both Pt and Pb (**Fig. 11(a)** and (**b**)) measured across two adjacent nanoparticles (as indicated in **Fig. 10**) also indicate a core–shell type structure with a Pt shell and a Pb core. Similar behavior for EDX line scan measurements of Pt core–shell nanoparticles have been reported in the literature [50,51].

4. Conclusions

A new method for the synthesis of carbon supported core–shell nanostructures ($\text{Pb}_x@\text{Pt}_y/\text{C}$) has developed. Thus, $\text{Pb}_x@\text{Pt}_y/\text{C}$ core–shell nanostructures with well-defined morphologies were successfully synthetized for the first time. The formation of core–shell structures for the $\text{Pb}@\text{Pt}_3/\text{C}$ was confirmed by CV, HAADF-STEM and EDX measurements. XRD and XPS data confirmed the presence of metallic Pt and Pb, as well as the presence PbO_2 for all synthetized catalysts. Electrochemical measurements indicated that the catalytic activity towards glycerol oxidation depends on the composition and structure of the catalysts. The superficial area of the $\text{Pb}@\text{Pt}_3/\text{C}$ increased significantly in this structure, which enhanced, subsequently, the catalytic activity, generating high pseudo-current densities for glycerol oxidation. Thus, the highest catalytic activity obtained at the $\text{Pb}@\text{Pt}_3/\text{C}$ electrocatalyst can be attributed to mechanical stress combined with electronic effects. The PbPt_3/C alloy is active toward the oxidation

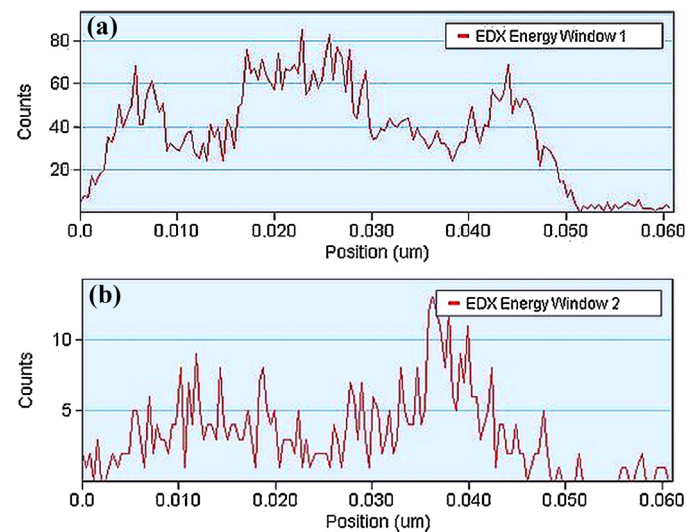


Fig. 11. EDX line scan profiles across the particles indicated in **Fig. 10** of the Pt shell in energy window 1 (upper spectrum) and Pb core in energy window 2 (lower spectrum).

of glycerol in an acid medium but it is not durable in realizing this process. In contrast, the CS nanostructure $\text{Pb}@\text{Pt}_3/\text{C}$ is promising for application in direct glycerol fuel cells as it exhibits a very good electrocatalytic activity for this process associated with a high stability. This catalyst demonstrated superior electrochemical stability after 3000 voltammetric cycles which was superior to the other investigated samples, including the Pt/C catalyst.

Acknowledgements

The authors thank the Brazilian National Council of Technological and Scientific Development-CNPq (grants: 303630/2012-4, 474261/2013-1, 407274/2013-8, 402243/2012-9, 400443/2013-9, 310282/2013-6 and 304419/2015-0), to CAPES and to FAPITEC for the scholarships and financial support for this work.

Appendix A. Supplementary data

Supplementary data associated with this article can be found, in the online version, at <http://dx.doi.org/10.1016/j.apcatb.2016.04.046>.

References

- [1] J.C.M. Silva, R.F.B. De Souza, L.S. Parreira, E. Teixeira Neto, M.L. Calegaro, M.C. Santos, *Appl. Catal. B: Environmental* 99 (2010) 265–271.
- [2] D. Morales-Acosta, D. López de La Fuente, L.G. Arriaga, G. Vargas Gutiérrez, F.J. Rodríguez Varela, *Int. J. Electrochem. Sci.* 6 (2011) 1835–1854.
- [3] M. Etesami, N. Mohamed, *Int. J. Electrochem. Sci.* 6 (2011) 4676–4689.
- [4] B. Xiong, Y. Zhou, Y. Zhao, J. Wang, X. Chen, R. O' Hayre, Z. Shao, *Carbon* 52 (2013) 181–192.
- [5] M.Z.F. Kamarudin, S.K. Kamarudin, M.S. Masdar, W.R.W. Daud, *Int. J. Hydrogen Energy* 38 (2013) 9438–9453.
- [6] B. Braunschweig, D. Hibbitts, M. Neurock, A. Wieckowski, *Catal. Tod.* 202 (2013) 197–209.
- [7] Y. Kajikawa, J. Yoshikawa, Y. Takeda, K. Matsushima, *Technol. Forecast. Soc. Change* 75 (2008) 771–782.
- [8] F. Ren, F. Jiang, Y. Du, P. Yang, C. Wang, J. Xu, *Int. J. Electrochem. Sci.* 6 (2011) 5701–5709.
- [9] W. Li, C. Liang, W. Zhou, J. Qiu, Zhenhua, G. Sun, Q. Xin, *J. Phys. Chem. B* 107 (2003) 6292–6299.
- [10] L. Zhang, D. Xia, *Appl. Surf. Sci.* 252 (2006) 2191–2195.
- [11] G. Li, L. Jiang, S. Wang, G. Sun, *Electrochim. Acta* 56 (2011) 7703–7711.
- [12] X. Zhao, M. Yin, L. Ma, L. Liang, C. Liu, J. Liao, T. Lu, W. Xing, *Energy Environ. Sci.* 4 (2011) 2736–2753.
- [13] L.J. Hobson, H. Ozu, M. Yamaguchi, S. Hayase, *J. Electrochem. Soc.* 148 (2001) A1185–A1190.

[14] H. Liu, C. Song, L. Zhang, J. Zhang, H. Wang, D.P. Wilkinson, *J. Power Sources* 155 (2006) 95–110.

[15] A. Heinzel, V.M. Barragán, *J. Power Sources* 84 (1999) 70–74.

[16] S. Song, W. Zhou, Z. Liang, R. Cai, G. Sun, Q. Xin, V. Stergiopoulos, P. Tsakarais, *Appl. Catal. B: Environmental* 55 (2005) 65–72.

[17] A. Nirmala Grace, K. Pandian, *Electrochem. Comm.* 8 (2006) 1340–1348.

[18] R.L. Arechederra, B.L. Treu, S.D. Minteer, *J. Power Sources* 173 (2007) 156–161.

[19] M. Simões, S. Baranton, C. Coutanceau, *Appl. Catal. B: Environmental* 93 (2010) 354–362.

[20] V. Bambagiano, C. Bianchini, A. Marchionni, J. Filippi, F. Vizza, J. Teddy, P. Serp, M. Ziani, *J. Power Sources* 190 (2009) 241–251.

[21] N. Atrux-Tallau, C. Romagny, A. Denis, M. Haftek, M. Falson, F. Pirot, H.I. Maibach, *Arch. Dermatol. Res.* 302 (2010) 435–441.

[22] M. Schell, Y. Xu, Z. Zdravesci, *J. Phys. Chem.* 100 (1996) 18962–18969.

[23] S. Demirel, M. Lucas, J. Warna, T. Salmi, D. Murzin, P. Claus, *Top. Catal.* 44 (2007) 299–305.

[24] H.J. Kim, S.M. Choi, S. Green, G.A. Tompsett, S.H. Lee, G.W. Huber, W.B. Kim, *Appl. Catal. B: Environmental* 101 (2011) 366–375.

[25] H.B. Suffredini, G.R. Salazar-Banda, L.A. Avaca, *J. Power Sources* 171 (2007) 355–362.

[26] H.B. Suffredini, G.R. Salazar-Banda, L.A. Avaca, *J. Sol-Gel Sci. Technol.* 49 (2009) 131–136.

[27] G.R. Salazar-Banda, K.I.B. Eguiluz, M.M.S. Pupo, H.B. Suffredini, M.L. Calegaro, L.A. Avaca, *J. Electroanal. Chem.* 668 (2012) 13–25.

[28] Y. Huang, J. Cai, Y. Guo, *Int. J. Hydrogen Energy* 37 (2012) 1263–1272.

[29] S.C.S. Lai, S.E.F. Kleyn, V. Rosca, M.T.M. Koper, *J. Phys. Chem.* 112 (2008) 19080–19087.

[30] Z. Liu, B. Guo, S.W. Tay, L. Hong, X. Zhang, *J. Power Sources* 184 (2008) 16–22.

[31] E. Casado-Rivera, D.J. Volpe, L. Alden, C. Lind, C. Downie, T. Vázquez-Alvarez, A.C.D. Angelo, F.J. DiSalvo, H.D. Abruña, *J. Am. Chem. Soc.* 126 (2004) 4043–4049.

[32] G.A. Camara, R.B. Lima, T. Iwasita, *Electrochem. Comm.* 6 (2004) 812–815.

[33] G.A. Camara, R.B. Lima, T. Iwasita, *J. Electroanal. Chem.* 585 (2005) 128–131.

[34] I.N. Leontyev, D.Y. Chernyshov, V.E. Guterman, E.V. Pakhomova, A.V. Guterman, *Appl. Catal. A* 357 (2009) 1–4.

[35] J. Zhou, J. He, Y. Ji, G. Zhao, C. Zhang, X. Chen, T. Wang, *Acta Physico Chim. Sin.* 24 (2008) 839–843.

[36] E.G. Ciapina, S.F. Santos, E.R. Gonzalez, *J. Electroanal. Chem.* 644 (2010) 132–143.

[37] S.-B. Han, Y.-J. Song, J.-M. Lee, J.-Y. Kim, K.-W. Park, *Electrochem. Comm.* 10 (2008) 1044–1047.

[38] E.G. Ciapina, S.F. Santos, E.R. Gonzalez, *J. Solid State Electrochem.* 17 (2013) 1831–1842.

[39] H.J. Kim, S.M. Choi, M.H. Seo, S. Green, G.W. Huber, W.B. Kim, *Electrochem. Comm.* 13 (2011) 890–893.

[40] T.S. Almeida, L.M. Palma, P.H. Leonello, C. Morais, K.B. Kokoh, A.R. de Andrade, *J. Power Sources* 215 (2012) 53–62.

[41] L. Zhao, J.P. Thomas, N.F. Heinig, M. Abd-Ellah, X. Wang, K.T. Leung, *J. Mater. Chem. C* 2 (2014) 2707–2714.

[42] G.S. Buzzo, M.J.B. Orlandi, E. Teixeira-Neto, P. Homem-de-Mello, A.C.G. Lopes, E. Franco-Junior, H.B. Suffredini, *J. Power Sources* 199 (2012) 75–84.

[43] X. Wang, L. Altmann, J. Stover, V. Zielasek, M. Baumer, K. Al-Shamery, H. Borchert, J. Parisi, J. Kolny-Olesiak, *Chem. Mater.* 25 (2013) 1400–1407.

[44] J.-H. Song, J.-Y. Yu, M.-Z. Zhang, Y.-J. Ling, C.-W. Xu, *Int. J. Electrochem. Sci.* 7 (2012) 4362–4368.

[45] A. Sadiki, P. Vo, S. Hu, T.S. Copenhaver, L. Scudiero, S. Ha, J.L. Haan, *Increased Electrochemical Oxidation Rate of Alcohols in AlkalineMedia on Palladium Surfaces Electrochemically Modified by Antimony, Lead, and Tin*, *Electrochim. Acta* 139 (2014) 302–307.

[46] S. Sun, G. Zhang, D. Geng, Y. Chen, R. Li, M. Cai, X. Sun, *Angew. Chem.* 123 (2011) 442–446.

[47] L.L.A. Souza, G.R.O. Almeida, L.S.R. Silva, F.O.F. Bergamaski, A.S. Lima, K.I.B. Eguiluz, G.R. Salazar-Banda, *J. Appl. Electrochem.* 43 (2013) 953–965.

[48] S.G. Lemos, R.T.S. Oliveira, M.C. Santos, P.A.P. Nascente, L.O.S. Bulhões, E.C. Pereira, *J. Power Sources* 163 (2007) 695–701.

[49] J.P.I. Souza, T. Iwasita, F.C. Nart, W. Vielstich, *J Appl Electrochem* 30 (1999) 43–48.

[50] M. Heggen, M. Oezaslan, L. Houben, P. Strasser, *J. Phys. Chem. C* 116 (2012) 19073–19083.

[51] D.A. Cantane, F.E.R. Oliveira, S.F. Santos, F.H.B. Lima, *Appl. Catal. B: Environmental* 136–137 (2013) 351–360.

[52] Z.H. Long, X.M. Tao, H.S. Liu, Z.P. Jin, *J. Phase Equilib.* 30 (2009) 318–322.

[53] D.H. Youn, S. Han, G. Bae, J.S. Lee, *Electrochem. Comm.* 13 (2011) 806–809.

[54] K. Shimizu, I.F. Cheng, C.M. Wai, *Electrochem. Comm.* 11 (2009) 691–694.

[55] F.H.B. Lima, W.H. Lizcano-Valbuena, E. Teixeira-Neto, F.C. Nart, E.R. Gonzalez, E.A. Ticianelli, *Electrochim. Acta* 52 (2006) 385–393.

[56] C. Li, Y. Yamauchi, *Phys. Chem. Chem. Phys.* 15 (2013) 3490–3496.

[57] J. Wu, Y.-T.P. Li, X. Yin, H. Yang, *Chem. Soc. Rev.* 41 (2012) 8066–8074.

[58] F. Maillard, E.R. Savinova, U. Stimming, *J. Electroanal. Chem.* 599 (2007) 221–232.

[59] J. Jiang, A. Kucernak, *J. Electroanal. Chem.* 533 (2002) 153–165.

[60] O.V. Cherstiouk, P.A. Simonov, E.R. Savinova, *Electrochim. Acta* 48 (2003) 3851–3860.

[61] S. Guerin, B.E. Hayden, C.E. Lee, C. Mormiche, J.R. Owen, A.E. Russell, B. Theobald, D. Thompsett, *J. Comb. Chem.* 6 (2004) 49–158.

[62] S. Alayoglu, A.U. Nilekar, M. Mavrikakis, B. Eichhorn, *Nat. Mater.* 7 (2008) 333–338.

[63] N. Kristian, X. Wang, *Electrochem. Comm.* 10 (2008) 12–15.

[64] K. Hiroshima, T. Asaoka, T. Noritake, Y. Ohya, Y. Morimoto, *Fuel Cells* 2 (2002) 31–34.

[65] J.K. Nørskov, J. Rossmeisl, A. Logadottir, L. Lindqvist, *J. Phys. Chem. B* 108 (2004) 17886–17892.

[66] J.X. Wang, C. Ma, Y.M. Choi, D. Su, Y. Zhu, P. Liu, R. Si, M.B. Vukmirovic, Y. Zhang, R.R. Adzic, *J. Am. Chem. Soc.* 133 (2011) 13551–13557.

[67] J. Huang, Z. Liu, C. He, L.M. Gan, *J. Phys. Chem. B* 109 (2005) 16644–16649.

[68] L. Roquet, E.M. Belgisir, J.-M. Léger, C. Lamy, *Electrochim. Acta* 39 (1994) 2387–2394.

[69] Y. Kwon, Y. Birdja, I. Spanos, P. Rodriguez, M.T.M. Koper, *ACS Catal.* 2 (2012) 759–764.

[70] J.F. Gomes, G. Tremiliosi-Filho, *Electrocatal.* 2 (2011) 96–105.

[71] P.S. Fernández, C.A. Martins, M.E. Martins, G.A. Camara, *Electrochim. Acta* 112 (2013) 686–691.

[72] E.A. Batista, G.R.P. Malpass, A.J. Motheo, T. Iwasita, *Electrochem. Commun.* 5 (2003) 843–846.

[73] R.F.B. De Souza, L.S. Parreira, D.C. Rascio, J.C.M. Silva, E. Teixeira-Neto, M.L. Calegaro, E.V. Spinace, A.O. Neto, M.C. Santos, *J. Power Sources* 195 (2010) 1589–1593.

[74] R.T.S. Oliveira, M.C. Santos, B.G. Marcussi, P.A.P. Nascente, L.O.S. Bulhões, E.C. Pereira, *J. Electroanal. Chem.* 575 (2005) 177–182.

[75] R.T.S. Oliveira, M.C. Santos, B.G. Marcussi, S.T. Nanimoto, L.O.S. Bulhoes, E.C. Pereira, *J. Power Sources* 157 (2006) 212–216.

[76] R.G. Freitas, E.P. Antunes, E.C. Pereira, *Electrochim. Acta* 54 (2009) 1999–2003.

[77] B. Hammer, J.K. Nørskov, *Adv. Catal.* 45 (2000) 71–129.

[78] D. Kaplan, L. Burstein, Y. Rosenberg, E. Peled, *J. Power Sources* 196 (2011) 8286–8292.

[79] D. Mott, J. Luo, A. Smith, P.N. Njoki, L. Wang, C.-J. Zhong, *Nanoescale Res. Lett.* 2 (2007) 12–16.

[80] K. Bergamaski, E.R. Gonzalez, F.C. Nart, *Electrochim. Acta* 53 (2008) 4396–4406.

[81] S.-M. Hwang, J.E. Bonevich, J.J. Kim, T.P. Moffat, *J. Electrochem. Soc.* 158 (2011) B1019–B1028.

[82] F.E. López-Suárez, A. Bueno-López, K.I.B. Eguiluz, G.R. Salazar-Banda, *J. Sources Power* 268 (2014) 225–232.

[83] F.E. López-Suárez, M. Perez-Cadenas, A. Bueno-López, C.T. Carvalho-Filho, K.I.B. Eguiluz, G.R. Salazar-Banda, *J. Appl. Electrochem.* 45 (2015) 1057–1068.

[84] Y. Huang, J. Cai, Y. Guo, *Int. J. Hydrogen Energy* 37 (2012) 1263–1271.

[85] F.E. López-Suárez, C.T. Carvalho-Filho, A. Bueno-López, J. Arboleda, A. Echavarria, K.I.B. Eguiluz, G.R. Salazar-Banda, *Int. J. Hydrogen Energy* 40 (2015) 12674–12686.

[86] S.J. Pennycook, D.E. Jesson, A.J. McGibbon, P.D. Nellist, *J. Electron Microsc.* 45 (1996) 36–43.